FORMULATION OF AN ISOGEOMETRIC SHELL ELEMENT FOR CRASH SIMULATION

Cédric ADAM[1,3,*], Salim BOUABDALLAH[2], Malek ZARROUG[1] and Habibou MAITOURNAM[3]

[1]Direction Scientifique et Technologies Futures
PSA Peugeot Citroën
Route de Gisy, 78140 Vélizy-Villacoublay, France
e-mail: cedric.adam1@mpsa.com, malek.zarroug@mpsa.com

[2]Département Mécanique des Systèmes
École supérieure d'Ingénieurs Léonard de Vinci
8 avenue Léonard de Vinci, 92400 Courbevoie, France
e-mail: salim.bouabdallah@devinci.fr

[3]Laboratoire de Mécanique des Solides
École Polytechnique
Route de Saclay, 91128 Palaiseau, France
e-mail: maitournam@lms-polytechnique.fr

Key words: isogeometric analysis, linear hardening, non-linearities, NURBS, Reissner-Mindlin, shells.

Abstract. In this paper, we propose, for the isogeometric analysis, a shell model based on a degenerated three dimensional approach. It uses a first order kinematic description in the thickness with transverse shear (Reissner-Mindlin theory). We examine various approaches to describe the geometry and compare them on various linear and non-linear benchmark problems. Both geometric and material non-linearities are treated. The obtained results are compared with the solutions of isogeometric solid model and with other numerical solutions found in the literature.

1 INTRODUCTION

The predictive capability in car crash numerical simulation is increasingly expected and the high precision required leads to an explosion in computation time. The geometry proved to be very significant in this kind of explicit calculation, so it is often necessary to mesh some parts with small elements, which greatly penalizes the stable time step in finite element analysis (FEA). An interesting alternative is isogeometric analysis (IGA),

a method that allows to use exact geometry without necessarily using small elements as in FEA.

We are interested in IGA proposed by TJR Hughes et al. [1] and based on the exact geometry representation, as it is created in CAD software. The main objective of this emergent method is to closely link the two steps of design and analysis. The basis functions, B-Spline, NURBS (Non Uniform Rational B-Splines) and more recently T-Splines [2], are immediately provided by the CAD model.

2 BASIS FUNCTION

In this section, we shortly review the general concept of IGA, one can find further details in [4]. NURBS are the most popular tools to generate curves, surfaces and volumes in nowadays CAD software.

Since B-Splines are polynomial functions, they cannot exactly represent circular arcs and other conic sections. NURBS generalize the concept of B-Splines and can exactly represent theses objects.

A basis of univariate B-Splines functions of order p is defined by a knot vector $\Xi = \{\xi_1, \ldots, \xi_{n+p+1}\}$. Ξ is a non-decreasing set of real numbers that represents the coordinates of the basis functions in the parametric space.

B-splines are calculated by a recursive formula:

$$\begin{aligned} \forall i \in [|1, n+p|] \qquad & N_{i,0}(\xi) = \chi_{[\xi_i, \xi_{i+1}[}, \\ \forall i \in [|1, n+p-k|], \forall k \in [|1, p|] \qquad & N_{i,k}(\xi) = \frac{\xi - \xi_i}{\xi_{i+k} - \xi_i} N_{i,k-1}(\xi) + \frac{\xi_{i+k+1} - \xi}{\xi_{i+k+1} - \xi_{i+1}} N_{i+1,k-1}(\xi) \end{aligned} \tag{1}$$

where $\chi_{[a,b]}$ is the indicator function of the interval $[a, b]$. Efficient algorithms such as Cox-de Boor formula can quickly evaluate the basis functions and their derivatives (see [4]).

These functions respect the partition of unity $\sum_i N_{i,k}(\xi) = 1$, a fundamental property that allows to use them for the numerical simulation. Their regularity between two parametric or physical elements is entirely defined by the multiplicity of the associate knot in the knot vector Ξ. This regularity r is given by $r = p - m$ where p is the order used for the basis functions and m the multiplicity of the knot ξ_i. In the case of $p = m$ we obtain a C^0 regularity, at the associated knot ξ_{i0} a single function is non zero and becomes interpolating.

The figure 1, on the left, illustrates these main properties of the Splines. On this example of univariate B-Splines with the order $p = 2$ and the knot vector $\Xi = \{0, 0, 0, 1, 2, 2, 3, 4, 5, 5, 5\}$ we have a maximum C^1 regularity excepted at the knot $\xi_i = 2$ where the regularity is only C^0. An important property illustrated in this example is that the first and the last knot must have a multiplicity $m = p + 1$ to have interpolating functions at the two ends, the knot vector is so called open knot vector.

A B-Spline curve is defined by a knot vector Ξ and n control points $\mathbf{X}_1, \ldots, \mathbf{X}_n$:

$$\mathbf{C}(\xi) = \sum_{i=1}^{n} N_{i,p}(\xi)\mathbf{X}_i. \tag{2}$$

Surfaces and volumes are constructed in a similar way. For instance, a surface will be defined by two knot vectors Ξ and H, and nm control points $\mathbf{X}_{11}, \ldots, \mathbf{X}_{nm}$:

$$\mathbf{S}(\xi, \eta) = \sum_{i=1}^{n}\sum_{j=1}^{m} N_{i,p}(\xi)M_{j,q}(\eta)\mathbf{X}_{ij}. \tag{3}$$

For sake of clarity, we will use a conventional indexing $N_A(\xi, \eta) = N_{i,p}(\xi)M_{j,q}(\eta)$. NURBS basis functions, noted $R_A(\xi, \eta)$, are defined by the control points weighted by the variable w_A. One can define a weight function $W(\xi, \eta) = \sum_{A=1}^{nm} N_A(\xi, \eta)w_A$, that leads to

$$\mathbf{S}(\xi, \eta) = \frac{\sum_{A=1}^{nn} N_A(\xi, \eta)w_A\mathbf{X}_A}{W(\xi, \eta)} = \sum_{A=1}^{nn} R_A(\xi, \eta)\mathbf{X}_A. \tag{4}$$

We can highlight that the variables w_A are not unknowns, but input parameters, defined by the geometric modelling in CAD.

The figure 1, on the right, represents a unit sphere formed by eight elements which are defined by bivariate NURBS basis functions of order two. One can notice that some control points are located on the parametric surface, this correspond to a C^0 regularity at these points, whereas other points are located *outside* the sphere.

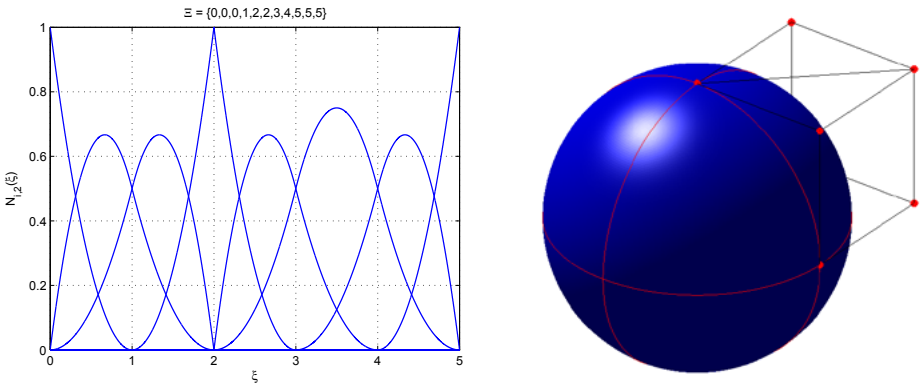

Figure 1: On the left, univariate B-Splines basis functions of order two with an open knot vector $\Xi = \{0, 0, 0, 1, 2, 2, 3, 4, 5, 5, 5\}$. On the right, NURBS sphere with a part of its control points (red points).

3 SHELL MODEL

In the present work, we propose a Reissner-Mindlin shell model, obtained from a degenerated three-dimensional model. We consider a first-order kinematic description in the thickness with transverse shear. There are six degrees of freedom, in the global coordinates system, at each control point (three translations and three rotations).

We consider a local plane stress state in the local coordinates system, i.e. $\sigma^l_{33} = 0$. The shells modelled here have a constant thickness h.

The Reissner-Mindlin theory is used in this context since it is more adapted to our industrial case. Transverse shear effects cannot be neglected without significantly deteriorate the numerical solution. Only a C^0 regularity is needed in a Reissner-Mindlin formulation but the isogeometric method can easily provides basis functions of higher continuity, required for a Kirchhoff-Love theory.

Our model differs from the work of DJ Benson et al. [3] by the normal description. The exact geometry of the shell is defined by

$$\mathbf{X}(\boldsymbol{\xi}) = \sum_{A=1}^{nm} R_A(\xi,\eta)\mathbf{X}_A + \frac{h}{2}\zeta\mathbf{n}(\xi,\eta), \tag{5}$$

where $\mathbf{x} = (x, y, z)^{\mathrm{T}}$ is the position vector of a point of the shell, $\boldsymbol{\xi} = (\xi, \eta, \zeta)^{\mathrm{T}}$ is the associated vector in the parametric space, R_A is the NURBS basis function associated to the control point $\mathbf{X}_A$, h the thickness and $\mathbf{n}$ the normal vector to the shell mid-surface at the point $\mathbf{X}$. ξ (resp. η) is defined by the knot vector Ξ (resp. H), whereas $\zeta \in [-1, 1]$ describes the thickness of the shell.

The interpolated displacements and the exact geometry of the shell are described by the same basis functions, that is

$$\mathbf{u}(\boldsymbol{\xi}) = \sum_{A=1}^{nm} R_A \left(\mathbf{U}_A + \frac{h}{2}\zeta\boldsymbol{\theta}_A \wedge \mathbf{n} \right), \tag{6}$$

where $\boldsymbol{\theta}_A$ is the rotation vector at the control point $\mathbf{X}_A$. One should notice that these displacements are only valid for small rotations if we use a total Lagrangian (TL) formulation. In this particular case, the simple relation $(\mathbf{R}(\boldsymbol{\theta}_A) - \mathbf{I}_3)\mathbf{n} \simeq \boldsymbol{\theta}_A \wedge \mathbf{n}$ remains true. If the geometry is often updated in the TL formulation or if an updated Lagrangian (UL) formulation is used then the rotation vector presented here is valid even for large rotations.

We consider several characterizations of the normal vector $\mathbf{n}$, exact or interpolated from its values at the control points, and we compare the performance of the different models for linear elastic test cases. The isogeometric method can provide an exact normal

$$\mathbf{u}(\boldsymbol{\xi}) = \sum_{A=1}^{nm} R_A \left(\mathbf{U}_A + \frac{h}{2}\zeta\boldsymbol{\theta}_A \wedge \mathbf{n} \right), \tag{7}$$

with

$$\mathbf{n} = \frac{\mathbf{X}_{,\xi} \wedge \mathbf{X}_{,\eta}}{||\mathbf{X}_{,\xi} \wedge \mathbf{X}_{,\eta}||_2}, \tag{8}$$

that requires the calculation of the first derivatives of the position vector in the shell formulation. The normal can also be interpolated from the values at the control points. This is immediate for the control points located on the geometry but for the other ones one have to define a different normal vector. In this work we will consider the normal definition of the orthogonal projection of the considered control point on the shell mid-surface. Several methods are presented and compared in [5]. The interpolated displacements become

$$\mathbf{u}(\boldsymbol{\xi}) = \sum_{A=1}^{nm} R_A \left(\mathbf{U}_A + \frac{h}{2} \zeta \boldsymbol{\theta}_A \wedge \mathbf{n}_A \right), \tag{9}$$

We define two tangent vectors (see [6]) $\mathbf{a}_1^{\text{cov}} = \mathbf{X}_{,\xi}$ and $\mathbf{a}_2^{\text{cov}} = \mathbf{X}_{,\eta}$, in order to construct a local orthonormal basis

$$\mathbf{n} = \frac{\mathbf{a}_1^{\text{cov}} \wedge \mathbf{a}_2^{\text{cov}}}{||\mathbf{a}_1^{\text{cov}} \wedge \mathbf{a}_2^{\text{cov}}||_2} \; ; \; \mathbf{t}_1 = \frac{\mathbf{a}_1^{\text{cov}}}{||\mathbf{a}_1^{\text{cov}}||_2} \; ; \; \mathbf{t}_2 = \mathbf{n} \wedge \mathbf{t}_1. \tag{10}$$

The construction of this basis is not unique, we could also change the definitions of the two vectors $\mathbf{t}_1$ and $\mathbf{t}_2$ or use a co-rotational approach as presented in [3]. We thus define the transformation matrix $\mathbf{P} = [\mathbf{t}_1, \mathbf{t}_2, \mathbf{n}]$, from the global to the local basis, for each calculation point.

For sake of clarity, square brackets will be used for the stress and strain tensors whereas their equivalent form in Voigt notation will be written without square brackets. We also use the superscript g (resp. l) to define a quantity in the global coordinates system (resp. local).

The small strain tensor is

$$[\boldsymbol{\epsilon}^g] = \frac{1}{2} \left(\mathbf{u}_{,\mathbf{X}} + \mathbf{u}_{,\mathbf{X}}^{\mathrm{T}} \right). \tag{11}$$

To respect the plane stress condition $\sigma_{33}^l = 0$, we use the transformation matrix

$$[\boldsymbol{\epsilon}^g] = \mathbf{P}[\boldsymbol{\epsilon}^l]\mathbf{P}^{\mathrm{T}} \; ; \; \; [\boldsymbol{\sigma}^g] = \mathbf{P}[\boldsymbol{\sigma}^l]\mathbf{P}^{\mathrm{T}}. \tag{12}$$

These relations are transformed using Voigt notation, i.e. $\boldsymbol{\sigma}^g = \mathbf{Q}\boldsymbol{\sigma}^l$ and $\boldsymbol{\epsilon}^l = \mathbf{Q}^{\mathrm{T}}\boldsymbol{\epsilon}^g$. We can now define the tangent constitutive matrix $\mathbf{C}_t^g = \mathbf{Q}\mathbf{C}_t^l\mathbf{Q}^{\mathrm{T}}$ in the global coordinates system.

The gradient matrix $\mathbf{F}_\zeta$ of the transformation between the parametric and the physical spaces is

$$\mathbf{F}_\zeta = \left[\begin{array}{ccc} \mathbf{X}_{,\xi} & \mathbf{X}_{,\eta} & \frac{h}{2}\mathbf{X}_{,\zeta} \end{array} \right] = \mathbf{F}_{\zeta=\mathbf{0}} + \frac{h}{2} \left[\begin{array}{ccc} \mathbf{n}_{,\xi} & \mathbf{n}_{,\eta} & 0 \end{array} \right]. \tag{13}$$

The Jacobian matrix $\mathbf{J}_\mathbf{X}$ of the transformation is

$$\mathbf{J}_\mathbf{X} = \mathbf{F}_\zeta^{\mathrm{T}} = \mathbf{X}_{,\boldsymbol{\xi}} = \sum_{A=1}^{nm} R_{A,\boldsymbol{\xi}} \mathbf{X}_A^{\mathrm{T}} + \frac{h}{2} (\zeta \mathbf{n})_{,\boldsymbol{\xi}}, \tag{14}$$

that enables to calculate $R_{A,\mathbf{X}} = \mathbf{J}_{\mathbf{X}}^{-1} R_{A,\boldsymbol{\xi}}$ and $\tilde{R}_{A,\mathbf{X}} = \mathbf{J}_{\mathbf{X}}^{-1} \tilde{R}_{A,\boldsymbol{\xi}}$, where $\tilde{R}_A = \frac{h}{2}\zeta R_A$, required for the computation of the strains.

Let $\mathbf{U}$ be the vector corresponding to the nodal degrees of freedom at the control points. We introduce the matrix $\mathbf{B}_L = \left[\begin{array}{cccc} \mathbf{B}_1 & \cdots & \mathbf{B}_A & \cdots \quad \mathbf{B}_{nm} \end{array} \right]$, the connection between the deformations and the displacements, i.e. $\epsilon^g = \mathbf{B}_L \mathbf{U}$ with

$$\mathbf{B}_A = \begin{bmatrix} R_{A,X} & 0 & 0 & 0 & (\tilde{R}_A n^Z)_{,X} & -(\tilde{R}_A n^Y)_{,X} \\ 0 & R_{A,Y} & 0 & -(\tilde{R}_A n^Z)_{,Y} & 0 & (\tilde{R}_A n^X)_{,Y} \\ 0 & 0 & R_{A,Z} & (\tilde{R}_A n^Y)_{,Z} & -(\tilde{R}_A n^X)_{,Z} & 0 \\ R_{A,Y} & R_{A,X} & 0 & -(\tilde{R}_A n^Z)_{,X} & (\tilde{R}_A n^Z)_{,Y} & (\tilde{R}_A n^X)_{,X} - (\tilde{R}_A n^Y)_{,Y} \\ 0 & R_{A,Z} & R_{A,Y} & (\tilde{R}_A n^Y)_{,Y} - (\tilde{R}_A n^Z)_{,Z} & -(\tilde{R}_A n^X)_{,Y} & (\tilde{R}_A n^X)_{,Z} \\ R_{A,Z} & 0 & R_{A,X} & (\tilde{R}_A n^Y)_{,X} & (\tilde{R}_A n^Z)_{,Z} - (\tilde{R}_A n^X)_{,X} & -(\tilde{R}_A n^Y)_{,Z} \end{bmatrix} . \quad (15)$$

Finally, the internal force vector is given by

$$\mathbf{F}^i = \int_{V^0} \mathbf{B}_L^{\mathrm{T}} \mathbf{C}_t^g \epsilon^g \, \mathrm{d}V^0, \quad (16)$$

and the tangent stiffness matrix $\mathbf{K}_t$ is

$$\mathbf{K}_t = \int_{V^0} \mathbf{B}_L^{\mathrm{T}} \mathbf{C}_t^g \mathbf{B}_L \, \mathrm{d}V^0. \quad (17)$$

4 NON-LINEARITIES

Geometric and material non-linearities are two phenomena that we have to consider since large deformations and displacements occur in car crash simulations. Plastic deformations have a significant role because they allow the material to absorb a huge quantity of energy during the crash.

4.1 Geometric non-linearities

In the framework of the large displacements, we compare the TL and the UL formulation performances for the 3D model, used as a reference model. We briefly remind the TL formulation, further details can be found in [7]. The Green-Lagrange tensor is

$$[\mathbf{E}^{\mathrm{g}}] = \frac{1}{2} \left(\mathbf{u}_{,\mathbf{X}} + \mathbf{u}_{,\mathbf{X}}^{\mathrm{T}} + \mathbf{u}_{,\mathbf{X}}^{\mathrm{T}} \mathbf{u}_{,\mathbf{X}} \right). \quad (18)$$

Using the vector notation $\mathbf{E}^{\mathrm{g}}$ we can rewrite

$$\mathbf{E}^{\mathrm{g}} = \left(\mathbf{H} + \frac{1}{2} \mathbf{A}(\mathbf{u}) \right) \mathbf{G}\mathbf{U} \quad (19)$$

where the expressions of $\mathbf{H}$, $\mathbf{A}(\mathbf{u})$ and $\mathbf{G}$ are detailed in [7] page 138.

We introduce the matrix $\mathbf{B}_{NL} = (\mathbf{H} + \mathbf{A}(\mathbf{u}))\mathbf{G}$, given by the relation $\mathbf{E}^g = \mathbf{B}_{NL}\mathbf{U}$. The internal force vector is

$$\mathbf{F}^i = \int_{V^0} \mathbf{B}_{NL}^{\mathrm{T}} \mathbf{C}_t^g \mathbf{E}^g \, \mathrm{d}V^0, \tag{20}$$

and the tangent stiffness matrix $\mathbf{K}_t$ is

$$\mathbf{K}_t = \mathbf{K}_{t1} + \mathbf{K}_{t\sigma} = \int_{V^0} \mathbf{B}_{NL}(\mathbf{u})^{\mathrm{T}} \mathbf{C}_t^g \mathbf{B}_{NL}(\mathbf{u}) + \mathbf{G}^{\mathrm{T}} \hat{\mathbf{S}} \mathbf{G} \, \mathrm{d}V^0 \tag{21}$$

where $\hat{\mathbf{S}}$ is the augmented stress matrix

$$\hat{\mathbf{S}} = \begin{bmatrix} [\mathbf{S}] & \mathbf{0} & \mathbf{0} \\ \mathbf{0} & [\mathbf{S}] & \mathbf{0} \\ \mathbf{0} & \mathbf{0} & [\mathbf{S}] \end{bmatrix}. \tag{22}$$

The first term $\mathbf{K_{t1}}$ is the "initial displacements" of the tangent stiffness matrix and the second term $\mathbf{K_{t\sigma}}$ is the "initial stresses".

4.2 Material non-linearities

In this section, we consider material non-linearities with elasto-plastic constitutive laws and in particular a Von Mises three dimensional plasticity model with linear kinematic and isotropic hardening in the context of small strains. It is convenient to introduce deviatoric and volumetric parts of the strain $\boldsymbol{\epsilon}^g$ and stress $\boldsymbol{\sigma}^g$ vectors. Further details for the equations of the model can be found in [8].

A radial return method is used to solve the plasticity equations. Let the deviatoric strain be $\boldsymbol{e}_n$, the deviatoric stress $\boldsymbol{s}_n$, the plastic strain $\boldsymbol{\epsilon}_n^p$ and the total strain $\boldsymbol{p}$. We assume all these quantities known at time t_n and the deviatoric strain $\boldsymbol{e}_{n+1}$ at time t_{n+1}.

We first calculate the elastic trial step $(\mathbf{e}_{n+1}^{trial}, \mathbf{s}_{n+1}^{trial}, \boldsymbol{\epsilon}_{n+1}^{p,trial}, p_{n+1}^{trial})$ and if the new stress is admissible, i.e.

$$f = ||\mathbf{s}_{n+1}^{trial} - H_{kin}\boldsymbol{\epsilon}_{n+1}^{p,trial}|| - \sqrt{\frac{2}{3}}\left(\sigma_{y,0} + H_{iso}p_{n+1}^{trial}\right) \leqslant 0 \tag{23}$$

where $\sigma_{y,0}$ is the initial yield stress,H_{iso} and H_{kin} are two material constants, then the trial stress becomes the stress at time t_{n+1}. If the yield limit is violated, we introduce a

plastic correction

$$\begin{aligned}
\mathbf{e}_{n+1} &= \mathbf{e}_{n+1}^{trial} - \lambda \frac{\boldsymbol{\xi}}{||\boldsymbol{\xi}||}, \\
\mathbf{s}_{n+1} &= \mathbf{s}_{n+1}^{trial} - 2\mu\lambda \frac{\boldsymbol{\xi}}{||\boldsymbol{\xi}||}, \\
\boldsymbol{\epsilon}_{n+1}^{p} &= \boldsymbol{\epsilon}_{n+1}^{p,trial} + H_{kin}\lambda\boldsymbol{\xi}, \\
p_{n+1} &= p_{n+1}^{trial} + \lambda, \\
\lambda &= \frac{||\xi|| - \sqrt{\frac{2}{3}}\left(\sigma_{y,0} + H_{iso}p_{n+1}^{trial}\right)}{2\mu + H_{kin} + \sqrt{\frac{2}{3}}H_{iso}}, \\
\xi &= \mathbf{s}_{n+1}^{trial} - H_{kin}\boldsymbol{\epsilon}_{n+1}^{p,trial}.
\end{aligned} \tag{24}$$

We can now use two strategies: it is possible to update all the variables, create a new plastic force $\mathbf{F}^{plas}$ and solve the new problem

$$\mathbf{K}\mathbf{U}_{n+1} = \mathbf{F}^{ext} + \mathbf{F}_{n}^{plas}, \tag{25}$$

or we can also construct the algorithmically consistent tangent matrix $\mathbf{C}_{n}^{plas}$ and solve the system

$$\mathbf{K}_{n}^{plas}\mathbf{U}_{n+1} = \mathbf{F}^{ext}. \tag{26}$$

The second solution provides a better convergence of the Newton algorithm and we have to do fewer iterations at each time step, the construction of the stiffness matrix is expensive in IGA due to the high order of basis functions, the stiffness matrix is less sparse than the one obtained in FEA. The first solution needs to evaluate more plastic forces but we can keep the stiffness constant, which greatly reduce the cost in computation time of an iteration.

5 NUMERICAL RESULTS

We will evaluate our shell element on several well-known examples in linear and non-linear elasto-plasticity. The validation of these different quasi-static tests is an important process before using this element in explicit calculations.

5.1 Linear model

The performance of the linear shell model is evaluated using several benchmark problems in which analytical or numerical solutions are well known and can be considered as reference solutions [6] among others. For a benchmark in linear elasticity, one can find in the bibliography and for instance in [6] these different tests.

Several examples are presented in this paper and allows us to evaluate the precision of the shell model presented in the previous section. The obtained solutions are compared to the reference solutions and also to the 3D model we develop.

The first test is known as the Scordelis-Lo roof problem. It features a cylindrical panel supported by two rigid diaphragms at its ends and subjected to its own weight. Geometrical properties are $\frac{R}{h} = 100$ and $\frac{L}{h} = 200$, hence the roof is a thin shell. The transverse shear is negligible and the membrane deformations prevail over the bending deformations. Due to the symmetry of the problem, only a quarter of the shell (area ABCD on the figure 2) is modelled and simulated. We examine the vertical displacement of the point C located at the center of the cylindrical panel.

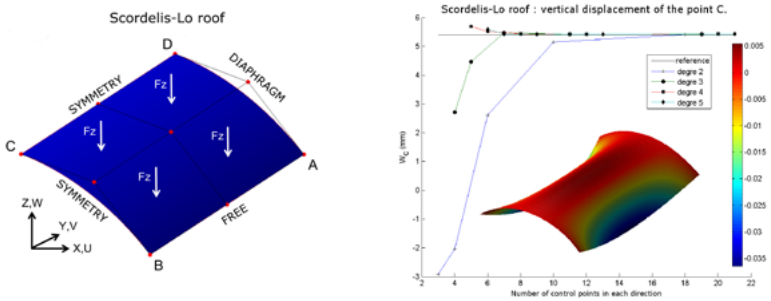

Figure 2: On the left, initial geometry and boundary conditions. On the right, vertical displacement of the point C and deformed geometry (scale factor $f = 20$).

The next problem is a pinched cylinder with two rigid diaphragms at its ends. The geometry of the cylindrical shell exhibits the same shape ratios as in the previous problem. This is a severe test case to evaluate the capacity of the shell element to describe the membrane and bending deformations, especially close to the points where the forces are applied. Only one eighth of the structure (area ABCD on the figure 3) is modelled. We examine the vertical displacement of the point C located at the center of the cylinder.

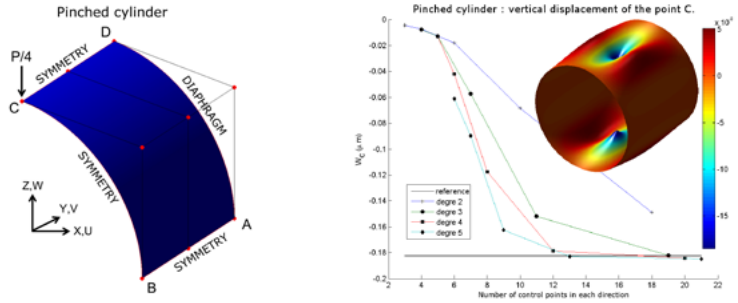

Figure 3: On the left, initial geometry and boundary conditions. On the right, vertical displacement of the point C and deformed geometry (scale factor $f = 5.10^6$).

The last linear elastic test presented here is a pinched hemispheric shell with a slenderness ratio $\frac{R}{h} = \frac{1}{250}$. This test ensures that the element does not suffer from membrane

locking. A quarter of the hemisphere (area ABCD on the figure 4) is modelled. We examine the horizontal displacement of the point A located at the base of the hemisphere.

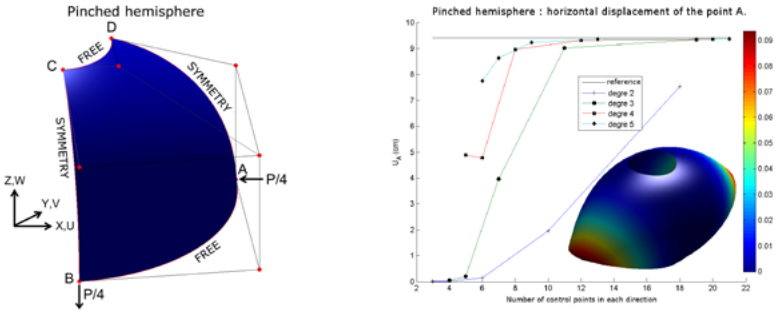

Figure 4: On the left, initial geometry and boundary conditions. On the right, horizontal displacement of the point A and deformed geometry (scale factor $f = 50$).

5.2 Geometric non-linearities

There are different test cases with geometric non-linearities and elastic constitutive laws. A complete benchmark referencing numerical solutions is detailed in [9]. We compare the precision and the convergence of the TL and UL formulations and compare our numerical solutions with the load-displacement curves given in [9].

The results are given for the geometric non-linear model of thick shell with sixteen elements in each direction. The 3D model gives the same results with only one element of order two in the thickness, more elements in the thickness or an higher order would not significantly ameliorate the precision but would greatly deteriorate the computation time.

Figure 5 shows the boundary conditions and the load-displacement curves for the pinched free hemisphere (on the left) and the stretched free cylinder (on the right). The cylinder test is more difficult to simulate since there is a change in the concavity of the solution for $P \simeq P_{max}/2$.

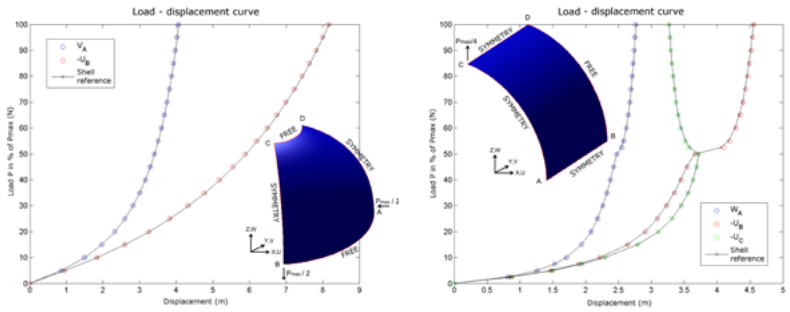

Figure 5: On the left, pinched free hemisphere. On the right, stretched free cylinder.

5.3 Material non-linearities

We have tested the 3D model on a rod with one element of order one. The rod is entirely free except for two sides on which we apply symmetric boundary conditions in order to obtain homogeneous stress in the element. The figure 6 illustrates a cyclic load of traction and compression with only kinematic hardening (on the left) and with isotropic-kinematic hardening (on the right).

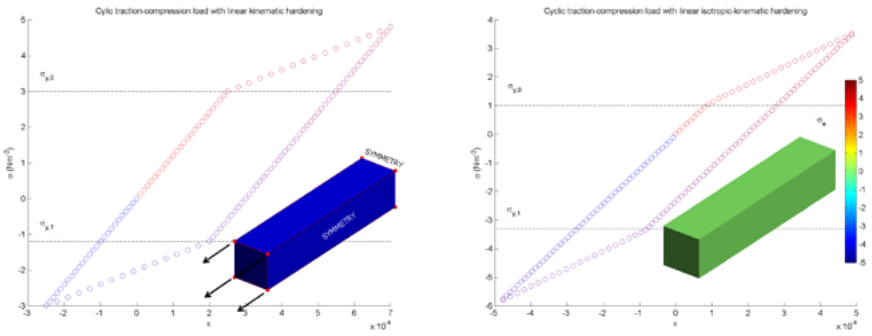

Figure 6: On the left, traction-compression cycle with linear kinematic hardening with the initial yield stress $\sigma_{y,0} = 3$. On the left, traction-compression cycle with linear isotropic-kinematic hardening with the initial yield stress $\sigma_{y,0} = 1$.

6 CONCLUSIONS AND FUTURE WORK

B-Splines and NURBS given by the geometric description of the modelled object during the CAD step are good candidates for the numerical analysis. In the industrial context of car crash simulation, the geometry is as complex as significant in the simulation process. Two of the main advantages of the IGA is to use the exact geometry for the analysis and to avoid the long process of meshing. The T-Splines have not been presented in this paper, we limit our work on relatively simple geometry described by B-Splines and NURBS but they would be a good alternative for more realistic geometries.

The linear elastic benchmark tests illustrate the fact that the higher order the shell element is, the less it suffers from membrane and shear locking that appears in thick shell elements. Several methods exist to unlock a curved thick beam element such as the Discrete Strain Gap method detailed in [10] and the B-bar method (see [11]) and can be adapted for shells.

Using high order elements to limit the locking phenomenon leads to a large number of integration point to integrate the basis functions if a classical Gaussian quadrature is employed. In order to limit the computation time, an optimized Gaussian integration has been proposed in [12] for particular cases of open knot vectors. The method benefits from the high regularity of the basis functions to use fewer integration points.

The linear elastic benchmark tests are not sufficient to highlight a significant difference between the models with an exact or an approximated normal definition, except for a

coarse mesh. However, the geometric non-linear benchmark illustrated that the model with an exact normal is more precise and less expensive in computation time since the projection of the normal at the control points have to be done at each update of the geometry.

We have introduced a 3D Von Mises plasticity model with linear kinematic and isotropic hardening, we will extend this work to a plane stress plasticity model. In the context of IGA, the calculation of the stiffness matrix is expensive so that the formulation with updated plastic forces is more effective for our current tests. In a future work, we will examine the best strategy to adopt for the coupling between the geometric and the material non-linearities under the hypothesis of large deformations and small strains that often occurs with slender geometries such as shells.

REFERENCES

[1] T.J.R Hughes, J.A. Cottrell, Y. Bazilevs. *Isogeometric Analysis: CAD, finite elements, NURBS, exact geometry and mesh refinement*, Comput. Methods Appl. Mech. Engrg., Elsevier, 194, 4135-4195, 2005.

[2] T.W. Sederberg, J. Zheng, A. Bakenov, A. Nasri. *T-splines and T-NURCCSs*, ACM Trans. Graph, 22, 477-484, 2003.

[3] D.J. Benson, Y. Bazilevs, M.-C. Hsu, T.R.J. Hughes. *Isogeometric shell analysis: The Reissner-Mindlin shell*, Comput. Methods Appl. Mech. Engrg., Elsevier, 199, 276-289, 2010.

[4] J.A. Cottrell, T.R.J. Hughes, Y. Bazilevs. *Isogeometric Analysis: Toward Integration of CAD and FEA*, Wiley, 2009.

[5] D.J. Benson, Y. Bazilevs, M.-C. Hsu, T.R.J. Hughes. *A large deformation, rotation-free, isogeometric shell*, Comput. Methods Appl. Mech. Engrg., Elsevier, 200, 1367-1378, 2011.

[6] J.-L. Batoz, G. Dhatt. *Modélisation des structures par éléments finis. Volume 3 coques*, Hermès, 1992.

[7] M.A. Crisfield. *Non-linear Finite Element Analysis of Solids ans Structures. Volume 1 essentials*, Wiley, 1991.

[8] J.C. Simo, T.J.R. Hughes. *Computational Inelasticity*, Springer, 1998.

[9] K.Y. Sze, X.H. Liu, S.H. Lo. *Popular benchmark problems for geometric nonlinear analysis of shells*, Finite Elements in Analysis and Design, Elsevier, 40, 1551-1569, 2004.

[10] F. Koschnick, M. Bischoff, N. Camprubí, K.-U. Bletzinger. *The discrete strain gap method and membrane locking*, Comput. Methods Appl. Mech. Engrg, Elsevier, 194, 2444-2463, 2005.

[11] T. Elguedj, Y. Bazilevs, V.M. Calo, T.J.R. Hughes. $\bar{B}$ *and* $\bar{F}$ *projection methods for nearly incompressible linear and non-linear elasticity and plasticity using higher-order NURBS elements*, Comput. Methods Appl. Mech. Engrg, Elsevier, 197, 2732-2762, 2008.

[12] F. Auricchio, F. Calabr, T.J.R. Hughes, A. Reali, G. Sangalli. *A simple algorithm for obtaining nearly optimal quadrature rules for NURBS-based isogeometric analysis*, Comput. Methods Appl. Mech. Engrg, Elsevier, 249-252, 15-27, 2012.

[13] W. Dornisch, S. Klinkel, B. Simeon. *Isogeometric Reissner-Mindlin shell analysis with exactly calculated director vectors*, Comput. Methods Appl. Mech. Engrg, Elsevier, 253, 491-504, 2013.